Nano Res. 2010, 3(9): 620–631
DOI 10.1007/s12274-010-0022-8
Research Article

ISSN 1998-0124
CN 11-5974/O4

Aqueous Synthesis of Mesostructured $BiVO_4$ Quantum Tubes with Excellent Dual Response to Visible Light and Temperature

Yongfu Sun, Yi Xie (✉), Changzheng Wu, Shudong Zhang, and Shishi Jiang

Hefei National Laboratory for Physical Sciences at Microscale, University of Science and Technology of China, Hefei 230026, China

Received: 1 July 2010 / Revised: 19 July 2010 / Accepted: 20 July 2010

ABSTRACT

Analysis of the atomic structure of monoclinic $BiVO_4$ reveals its fascinating structure-related dual response to visible light and temperature. Although there have been a few reported studies of its responses to visible light and temperature, an understanding of the effects of quantum size, particle shape or specific exposed facets on its dual responsive properties remains elusive; this is primarily due to the limited availability of high-quality monodisperse nanocrystals with extremely small sizes and specific exposed facets. Herein, we describe a novel assembly–fusion strategy for the synthesis of mesostructured monoclinic $BiVO_4$ quantum tubes with ultranarrow diameter of 5 nm, ultrathin wall thickness down to 1 nm and exposed {020} facets, via a convenient hydrothermal method at temperatures as low as 100 ℃. Notably, the resulting high-quality quantum tubes possess significantly superior dual-responsive properties compared with bulk $BiVO_4$ or even $BiVO_4$ nanoellipsoids, and thus, show high promise for applications as visible-light photocatalysts and temperature indicators offering improved environmental quality and safety. This mild and facile methodology should be capable of extension to the preparation of other mesostructured inorganic quantum tubes with similar characteristics, giving a range of materials with enhanced dual-responsive properties.

KEYWORDS

Mesostructure, $BiVO_4$, quantum tubes, visible light, temperature

1. Introduction

Since the first report of the preparation of bismuth vanadate crystals in 1925 [1], tremendous effort has been dedicated to synthesize monoclinic $BiVO_4$ (m-$BiVO_4$) owing to its fascinating structure-related properties. The structure of m-$BiVO_4$ consists of corner-sharing BiO_8 dodecahedra and VO_4 tetrahedra (Fig. 1(a)) [2], and its calculated 2.2 eV band gap and structure-determined reversible color change at ca. 255 ℃ render it suitable as a non-toxic visible-light-responsive photocatalyst for the degradation of harmful pollutants and as a thermochromic material for indicating temperature; it thus, offers both potential benefits for the environment and improved safety [3–5]. Although there have been a few reported studies of its responses to visible light and temperature [3–7], an understanding of the effects of quantum size, particle shape or specific exposed facets on its dual-responsive properties remains elusive; this is primarily due to the limited availability of high-quality monodisperse nanocrystals with extremely small sizes and specific exposed facets. The hot-injection organometallic approach has shown great promise for the fabrication

Address correspondence to yxie@ustc.edu.cn

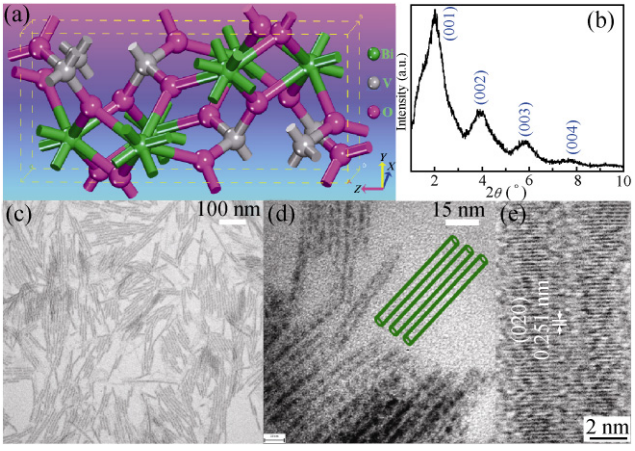

Figure 1 (a) Schematic unit cell structure of m-$BiVO_4$; (b) low-angle XRD pattern; (c, d) low and high magnification TEM images of mesostructured m-$BiVO_4$ quantum tubes, with the inset in (d) showing their tubular scheme; (e) high resolution TEM (HRTEM) image of a single quantum tube

of monodisperse quantum-sized nanocrystals [8, 9]. However, factors such as the high costs associated with the equipment for carrying out high-temperature oxygen-free reactions and the risks of using toxic organic solvents, will inevitably hinder practical application of this method. Accordingly, it is highly desirable to develop a facile and user-friendly strategy for synthesizing monodisperse quantum-sized m-$BiVO_4$ nanocrystals with specific shapes, in order to investigate their size and shape-related dual-responsive properties in the strong quantum confinement regime.

Herein, we describe a simple hydrothermal pathway to meet this challenge at temperatures as low as 100 ˚C, using non-toxic and inexpensive reagents such as bismuth nitrate and sodium oleate. This method allows monodisperse mesostructured m-$BiVO_4$ quantum tubes with ultranarrow diameter of 5 nm, ultrathin wall thickness down to 1 nm and exposed {020} facets to be synthesized for the first time. Encouragely, synergism between the ultranarrow diameter, ultrathin wall thickness and exposed {020} facets endow the m-$BiVO_4$ quantum tubes with significantly superior dual-responsive properties compared with bulk $BiVO_4$ or even m-$BiVO_4$ nanoellipsoids. The materials therefore show high promise for applications as visible-light photocatalysts and temperature indicators offering improved environmental quality and safety. This mild and facile methodology should be capable of extension to the preparation of other mesostructured inorganic quantum tubes with similar characteristics, giving a range of materials with greatly enhanced dual-responsive properties.

2. Experimental

2.1 Materials

$Bi(NO_3)_3{\cdot}5H_2O$, $Na_3VO_4{\cdot}12H_2O$, and sodium oleate were purchased from the Shanghai Reagent Company (China) and were used as obtained without further purification.

2.2 Synthesis

In a typical synthesis, sodium oleate (1.2 mmol) and $Bi(NO_3)_3{\cdot}5H_2O$ (0.4 mmol) were successively added to distilled water (20 mL). A solution of $Na_3VO_4{\cdot}12H_2O$ (0.4 mmol) in distilled water (20 mL) was then injected into the above solution. After vigorous stirring for 10 min, the mixture was transferred to a 50 mL Teflon-lined autoclave, sealed and heated at 100 ˚C for 12 h. The system was then allowed to cool down to room temperature.

2.3 Characterization and measurements

X-ray diffraction (XRD) patterns were recorded by using a Philips X'Pert PRO Super diffractometer with Cu *Kα* radiation (λ = 1.54178 Å). Tranmission electron microscope (TEM images) were obtained using a JEOL-2010 TEM with an acceleration voltage of 200 kV. Thermal gravimetric analysis (TGA) of the as-synthesized samples was carried out on a NETZSCH TG 209 F3 thermal analyzer from room temperature to 900 ˚C with a heating rate of 10 ˚C min^{-1} in N_2. Variable-temperature XRD patterns of the samples were recorded on a Shimadzu XRD-7000 diffractometer with Cu *Kα* radiation (λ = 1.54178 Å). Variable-temperature IR spectra were measured on a Nicolet FT-IR spectrometer. X-ray photoelectron spectra (XPS) were acquired on an ESCALAB MKII spectrometer with Mg *Kα* radiation (hυ = 1253.6 eV) as the excitation source. The binding energies obtained in the XPS spectral analysis were corrected for specimen charging by referencing C 1s to 284.5 eV. Differential scanning

calorimetry (DSC) cycling curves were measured using a NETZSCH DSC 200 F3 instrument with a heating/cooling rate of 10 ℃ min^{-1} between 20 ℃ and 500 ℃ in N_2. Brunauer–Emmett–Teller (BET) surface area was determined by nitrogen adsorption using a Micromeritics ASAP 2000 system. The photocatalytic performance of m-$BiVO_4$ quantum tubes was evaluated by the photodegradation of Rhodamine B under visible-light irradiation, which was provided by a commercial 500 W xenon lamp with a 380 nm cut-off filter. An aqueous suspension of $BiVO_4$ was prepared by adding powered $BiVO_4$ (0.6 mmol) to an aqueous solution of Rhodamine B (100 mL, 10^{-5} mol/L). The solution was protected from light and stirred for 6 h to reach adsorption equilibrium and uniform dispersion and was then exposed to visible light irradiation in air for 15 min. At 3 min intervals, the dispersion was filtered and the Rhodamine B concentration of the filtrate was determined using a UV/Vis-NIR spectrophotometer (Shimadzu SolidSpec-3700DUV).

3. Results and discussion

3.1 Characterization of the mesostructured m-$BiVO_4$ quantum tubes

The phase, chemical composition, and morphology of the as-obtained product can be revealed by XRD, XPS, and TEM, respectively. Thus, as shown in Fig. 2(a), the XRD pattern of the sample obtained at 100 ℃ for 12 h can be indexed as pure monoclinic scheelite $BiVO_4$ (JCPDS card 75-2480); interestingly, compared with the relative intensities shown in the standard pattern (Fig. 2(a)), the relatively strong 020 diffraction peak suggests that the as-synthesized products had a preferred growth orientation along the (020) direction. XPS analysis provided additional insights into the chemical composition of the product. The characteristic spin-orbit splitting of the Bi $4f_{5/2}$ and Bi $4f_{7/2}$ signals (bottom inset in Fig. 2(b)), V $2p_{1/2}$ and V $2p_{3/2}$ signals (top inset in Fig. 2(b)) and also the binding energies of the different elements are characteristic of monoclinic scheelite $BiVO_4$ [10]. Furthermore, the typical panoramic TEM image in Fig. 1(c) shows that the monodisperse m-$BiVO_4$ quantum tubes were formed on a large scale. Clearly, most of the quantum tubes are oriented parallel to one other, with an equal distance almost throughout the whole length of the structure, suggesting the formation of an ordered mesostructure. This was confirmed by the low-angle XRD pattern in Fig. 1(b). The series of low-angle XRD peaks can be assigned to "00*l*" (*l* = 1, 2, 3, 4…) reflections with a layer spacing of 4.41 nm, roughly the width of a bilayer of oleate ions [11–14]. The magnified TEM image (Fig. 1(d)) shows that the m-$BiVO_4$ quantum tubes have hollow structures, with a uniform ultranarrow diameter of ca. 5 nm and ultrathin wall thickness of ca. 1 nm. The continuous lattice spacing, nearly perpendicular to the tube walls, in the high resolution TEM (HRTEM) image (Fig. 1(e)) clearly shows that the quantum tubes possess good crystallinity. The lattice spacing was calculated to be 0.251 nm, corresponding

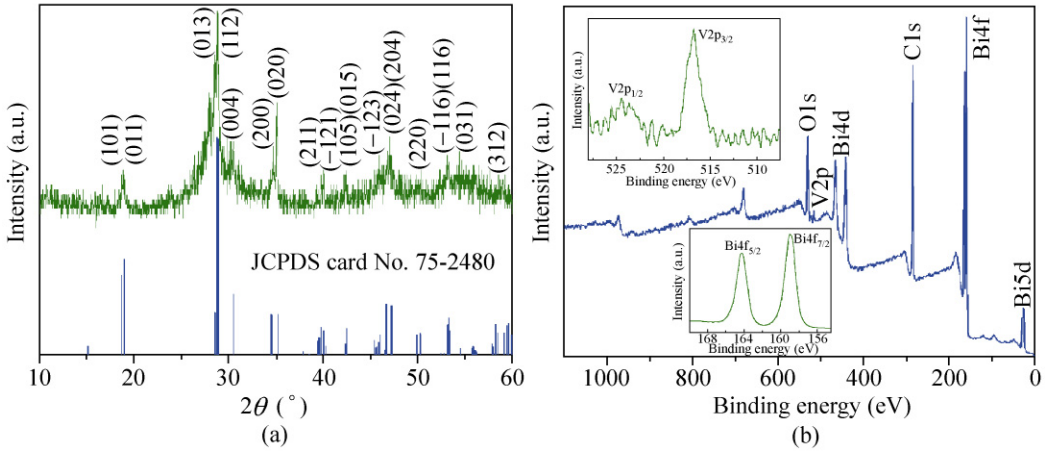

Figure 2 (a) Wide-angle XRD pattern and corresponding standard pattern of JCPDS card No. 75-2480; (b) XPS survey spectra for the product obtained at 100 ℃ for 12 h

to the (020) planes of m-$BiVO_4$, confirming the suggestion from XRD measurements that the well-crystallized quantum tubes have a preferred growth orientation along the (020) direction. Also, as depicted in Fig. S-1 in the Electronic Supplementary Material (ESM), the selected-area electron diffraction pattern recorded for a few m-$BiVO_4$ quantum tubes revealed an intense (020) diffraction, consistent with the HRTEM (Fig. 1(e)) and XRD (Fig. 2(a)) results. The above results all demonstrate that high-quality mesostructured m-$BiVO_4$ quantum tubes, with ultranarrow diameter, ultrathin wall thickness and exposed {020} facets, can be successfully synthesized via a mild and convenient hydrothermal method.

3.2 Mechanism of formation of mesostructured m-$BiVO_4$ quantum tubes

Time-dependent XRD patterns helped to demonstrate that the number of oleate ions attached and their peculiar arrangement around the surface of m-$BiVO_4$ played a vital role in the formation of mesostructured m-$BiVO_4$ quantum tubes, as shown in Scheme 1. Initially (Scheme 1(a)) each Bi^{3+} ion interacts electrostatically with three oleate ions to form Bi-oleate complexes, which then assemble into an ordered lamellar mesostructure (Scheme 1(b) and Fig. S-2 in the ESM) driven by the hydrophobic effect of the oleate tails [15]. Importantly, the presence of the Bi-oleate lamellar mesostructure was verified by the corresponding low-angle XRD pattern in Fig. 3(a). The periodicity of 4.71 nm is roughly twice the length of a fully stretched oleate ion, suggesting that oleate ions lie in a head-to-head (or tail-to-tail) bilayer arrangement [11]. After addition of Na_3VO_4 followed by hydrothermal treatment for 6 h, parallel pearl-necklace-shaped m-$BiVO_4$ quantum wires with a uniform spacing of sub-5 nm and diameter of ca. 1 nm (Scheme 1(c), Figs. 3(c) and 3(d)) were obtained. Interestingly, as shown by the low-angle XRD pattern in Fig. 3(b), these quantum wires also possessed an ordered meso-structure with a layer spacing of 4.54 nm, indicating that they retained the Bi-oleate lamellar mesostructure. As the reaction proceeded, these parallel pearl-necklace-shaped quantum wires tended to assemble together (as shown in Fig. 3(d)), mainly due to the associated reduction in surface energy [16], with a concomitant rearrangement of oleate ions on the surface of the $BiVO_4$ pearl-necklace-shaped quantum wires. Previous studies of the rearrangement of surfactant ions on the surface of polyoxometalates [17, 18] support our suggestion of oleate ion rearrangement on the surface of the $BiVO_4$ pearl-necklace-shaped quantum wires. As the $BiVO_4$ has three surface oleate ligands, it may be expected that the forces generated when $BiVO_4$ pearl-necklace-shaped quantum wires come into contact with each other result in the rearrangement of the oleate ions on the $BiVO_4$ surface leading to a Y-shaped arrangement—one oleate ion moves in one direction while the other two move in the opposite direction along the planes perpendicular to the pearl-necklace-shaped quantum wires (Scheme 1(d)). When the Y-shaped arrangements of oleate ions are aligned in the same direction, their mutual repulsion—coming from the direction of the pair of oleate ions—will inevitably force the side-to-side assembly of the pearl-necklace-shaped quantum wires to tilt a certain angle [17, 19], thus, making them gradually assemble into tubular nanostructures (Scheme 1(d) and 1(e)). Published reports of the formation of tubular or spherical shapes by polyoxometalates with three or four surfactant ions further support our assumption that the $BiVO_4$ quantum tubes are formed because of the specific number of oleate ions attached and their peculiar rearrangement [17, 18]. As shown in Fig. 1(d), the diameter of ca. 5 nm for the final quantum tubes is close to the 4.54 nm layer spacing of the pearl-necklace-shaped quantum wires and also the wall thickness of the quantum tubes (1 nm) is similar to the 1 nm diameter of the pearl-necklace-shaped quantum wires, consistent with the proposed assembly mechanism. Meanwhile, combining the above data and the simple geometric principle of $N = \pi D/d \approx 14$ (in which N and d are the number and diameter of pearl-necklace-shaped quantum wires and D is the diameter of the quantum tubes) suggests that about 14 pearl-necklace-shaped quantum wires were needed to assemble one quantum tube. It should be noted that in order to clearly show the assembly behaviour of the pearl-necklace-shaped quantum wires, only four quantum wires are actually shown in the formation of each quantum tube as depicted in Scheme 1(d). The corresponding detailed arrangement of the quantum

wires along the radial direction and wall direction of $BiVO_4$ quantum tube are displayed in Scheme 1(e), which shows that the pearl-necklace-shaped quantum wires gradually become tilted by a certain angle along the radial direction forming the tube-shaped structure; this is driven by the repulsive interactions between oleate ions in the outer direction. The pearl-necklace-shaped quantum wires remain parallel to each other along the wall direction and thus, form the wall of the $BiVO_4$ quantum tube. Here, it is worth noting that the walls of these newly formed quantum tubes are composed of single-layered loosely arranged pearl-necklace-shaped quantum wires, indicating that the ultrathin wall thickness of the quantum tubes is determined by the diameter of the pearl-necklace-shaped quantum wires. With increasing reaction time, the loosely arranged pearl-necklace-shaped quantum wires gradually fused into the final well-crystallized

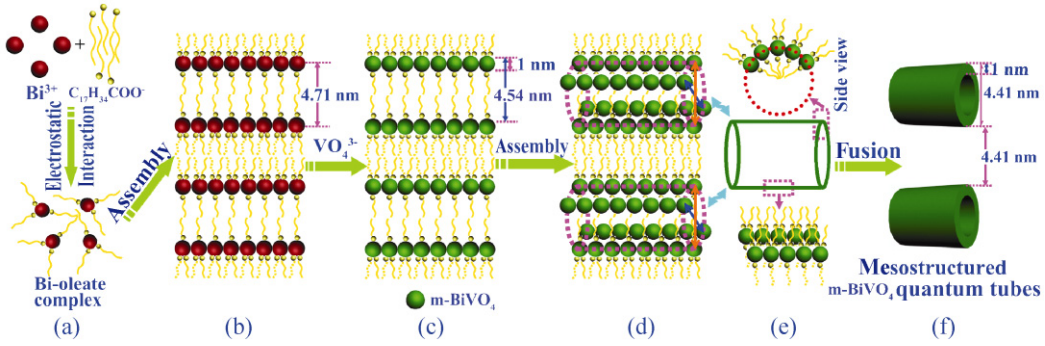

Scheme 1 Mechanism of formation of mesostructured m-$BiVO_4$ quantum tubes

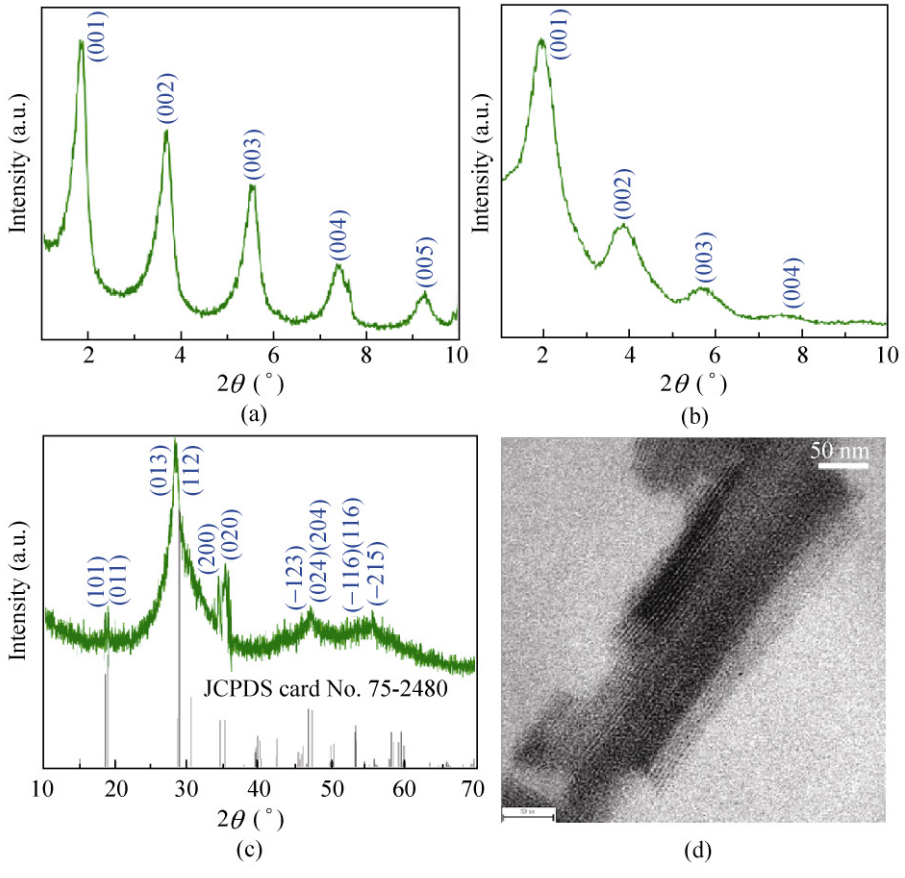

Figure 3 (a) Low-angle XRD pattern for Bi–oleate complexes; (b) low-angle; (c) wide-angle XRD patterns; (d) TEM image for m-$BiVO_4$ pearl-necklace-shaped quantum wires obtained at 100 °C for 6 h

walls [20, 21] (probably due to the associated reduction in surface energy [16]), as shown by the corresponding HRTEM image in Fig. 1(e). Of note, since the inner and outer surfaces of the quantum tubes are uniformly distributed by the bilayer arrangement of oleate ions (Scheme 1(d) and 1(e)), the final quantum tubes are necessarily parallel to one another and take on a monodisperse and ordered mesostructure, as shown by the corresponding low-angle XRD pattern in Fig. 1(b). Therefore, we believe that the formation of mesostructured m-$BiVO_4$ quantum tubes strongly depends on the number of attached oleate ions and the nature of their rearrangement on the surface of $BiVO_4$. The repulsive interactions between the Y-shaped arrangements of oleate ions provides the driving force for the formation of a tubular structure, while the specific bilayer arrangement of oleate ions on the inner and outer surfaces of the quantum tubes is responsible for their ultranarrow diameter and ordered mesostructure. Intriguingly, as many inorganic ions can form similar lamellar mesostructures with surfactant ions, this mechanism is potentially available to other inorganic compounds, which should allow a range of mesostructured quantum tubes with analogously ultranarrow diameter, ultrathin wall thickness and exposed special facets to be fabricated.

Before studying the response of the high-quality m-$BiVO_4$ quantum tubes to visible light and temperature, they were washed many times with ethanol and water, until the amount of oleate ions and adsorbed water reached a constant level of ca. 4.1%, as indicated by the TGA analysis in the following Fig. 6(e), in order to exclude any interference from surface oleate ions on the responsive properties.

3.3 Dual response of m-$BiVO_4$ quantum tubes to visible light and temperature

3.3.1 Visible-light-responsive photocatalysts for degradation of harmful organic pollutants

Visible-light-responsive photocatalysts are a highly promising means of degrading harmful organic pollutants, and can thus, help to alleviate the urgent environmental issues that confront mankind today. The crystal structure of m-$BiVO_4$, with its calculated band gap of 2.2 eV, makes it a promising visible-light-responsive photocatalyst [3]. In addition, DFT calculations suggest that the hybridization of Bi 6s and O 2p levels results in the valence band being highly delocalized, which favors the mobility of photo-excited holes and thus, enhances the photocatalytic oxidation of organic pollutants [22–24]. The optical absorption properties of m-$BiVO_4$, which are related to its electronic structure, are recognized as the key factors determining its photocatalytic activity [23, 25]. The UV-vis absorption spectrum of the m-$BiVO_4$ quantum tubes, shown in Fig. S-3(a) in the ESM, and the corresponding optical absorption edge shown in Fig. 4(a) indicate that they have a band gap energy of

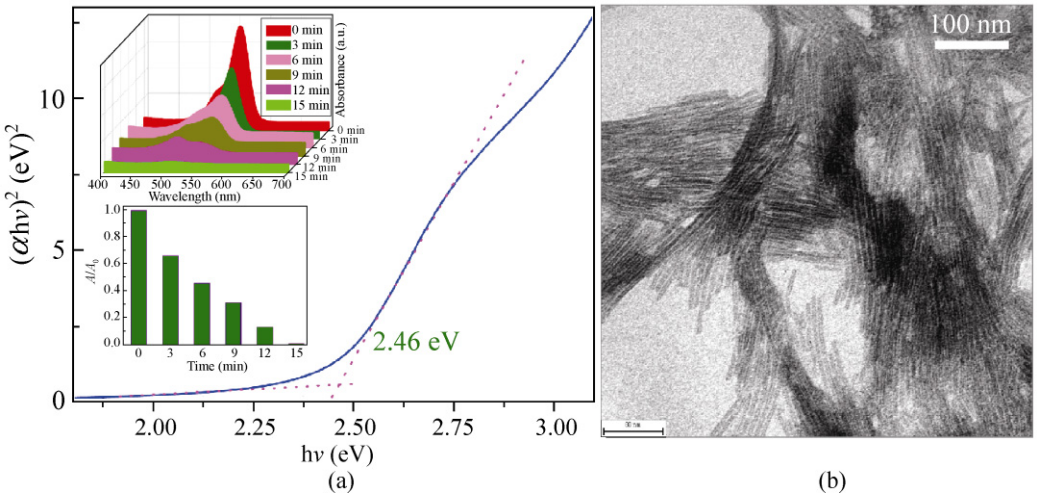

Figure 4 (a) Optical absorption edge of m-$BiVO_4$ quantum tubes; top and bottom insets: 3-D degradation and concentration change curves of Rhodamine B as a function of irradiation time ($\lambda > 400$ nm). (b) TEM image of m-$BiVO_4$ quantum tubes after the visible-light photodegradation of Rhodamine B

2.46 eV. The optical absorption edge and the band energy of m-$BiVO_4$ quantum tubes are significantly blue-shifted with respect to bulk $BiVO_4$, which may be ascribed to the quantum size confinement effect of the quantum tubes [3, 10, 26].

The photocatalytic activity of m-$BiVO_4$ quantum tubes was evaluated using Rhodamine B (RhB) photodegradation under visible light ($\lambda > 400$ nm) irradiation as a probe reaction. As shown in the top inset of Fig. 4(a), visible light absorption of the RhB/$BiVO_4$ suspension gradually decreased as a result of photodegradation under visible light irradiation. After 15 min, the extent of photodegradation of RhB reached 98.7% (Fig. 4(a)), over ten times larger than that achieved with TiO_2 (Degussa P25) (8%) or bulk-$BiVO_4$ (5.4%). The m-$BiVO_4$ quantum tubes were also roughly three times more active than m-$BiVO_4$ nanoellipsoids (for which photodegradation reached 96.6% in 45 min) [3]. The amount of RhB adsorbed on m-$BiVO_4$ quantum tubes in the dark was compared with the previously reported amounts for m-$BiVO_4$ nanoellipsoids and bulk-$BiVO_4$. As shown in Fig. S-3(b) in the ESM, there were no obvious differences between the amounts of RhB adsorbed by the three materials, indicating that the adsorption equilibrium in the dark does not have any influence on their effective photocatalytic activity. Furthermore, the morphology of m-$BiVO_4$ quantum tubes shows no obvious change after the photocatalytic reaction (Fig. 4(b)), confirming their good stability. The significantly enhanced photocatalytic activity of $BiVO_4$ quantum tubes can be attributed to its physical properties such as crystal size, BET surface area, and morphology. In particular, the ultranarrow diameter of 5 nm and ultrathin wall thickness of 1 nm could allow for more efficient transfer of electron–holes, generated inside the crystal, to the surface. Meanwhile, its extremely large surface area of 44.2 $m^2 \cdot g^{-1}$ (60 times higher than that of bulk $BiVO_4$ (0.7 $m^2 \cdot g^{-1}$)) will not only effectively promote the separation efficiency of the electron–hole pairs but also provide more active sites for the photocatalytic reaction; these both contribute to the higher quantum efficiency of the photocatalytic reaction [3, 25]. In addition, the uniformly exposed {020} facets of the m-$BiVO_4$ quantum tubes may supply more active sites compared with the randomly exposed facets in bulk $BiVO_4$, thus, improving its response to visible light. Accordingly, the synergism between the ultrathin wall thickness, large surface area and exposed {020} facets results in the m-$BiVO_4$ quantum tubes possessing significantly better visible-light-responsive photocatalytic properties than P25, bulk-$BiVO_4$ or even m-$BiVO_4$ nanoellipsoids, and make them attractive candidates for the degradation of harmful organic pollutants.

3.3.2 Temperature-induced thermochromism for indication of temperature

Recently, thermochromic materials have attracted significant attention due to their potential applications as environmentally benign temperature indicators in a wide range of devices such as cooking tools, furnaces, or car wheels offering improved safety. m-$BiVO_4$ is of interest for thermochromic applications since it possesses a reversible color change at ca. 255 ˚C, resulting from a reversible phase transition [4]. As mentioned above, the optical adsorption edge of the m-$BiVO_4$ quantum tubes shows a blue-shift with respect to that of bulk $BiVO_4$, owing to the quantum size confinement effect; this should have an impact on the color and affect the thermochromic properties of the material. On heating to 270 ˚C, the $BiVO_4$ quantum tubes underwent a striking color change from bright-yellow (20 ˚C) to brick-red (270 ˚C) (inset in Fig. 5(a)), which was more obvious than that for bulk-$BiVO_4$, which shows a color change between orange-yellow and light-red [3]. This color change was completely reversible when the samples were cooled in air and the color-recovery time was only several seconds.

The thermochromic property of $BiVO_4$ associated with its phase change was further studied by differential scanning calorimetry (DSC), variable-temperature XRD, variable-temperature IR spectroscopy, and TGA. As displayed in Fig. 5(a), sharp endothermic and exothermic peaks in the DSC curves, with higher transformation enthalpies than that of bulk-$BiVO_4$ [3], were observed at around the color change temperature for the m-$BiVO_4$ quantum tubes. These peaks showed no apparent change after ten cycles, indicating the good cyclability of m-$BiVO_4$ quantum tubes. Also, the morphology of the m-$BiVO_4$ quantum tubes (Fig. 5(b)) was unchanged after ten DSC cycles, confirming their

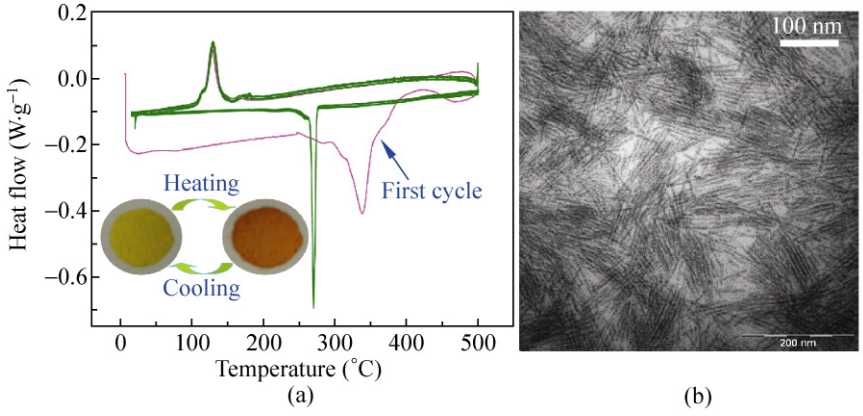

Figure 5 (a) DSC curves for ten cycles between 20 ˚C and 500 ˚C with a heating/cooling rate of 10 ˚C·min^{-1}; the inset image shows the striking reversible color change between 20 ˚C and 270 ˚C. (b) TEM image of m-$BiVO_4$ quantum tubes after the ten DSC cycles between 20 ˚C and 500 ˚C with a heating/cooling rate of 10 ˚C·min^{-1}

excellent thermal stability. Figure 5(a) illustrates that the m-$BiVO_4$ quantum tubes displayed a large thermal hysteresis phenomenon; the hysteresis width—the difference between the temperatures of maximal endothermic peak during heating (T_{ph}) and maximal exothermic peak during cooling (T_{pc})—was $\Delta T = T_{ph} - T_{pc} = 140$ K, similar to the value for m-$BiVO_4$ nanoellipsoids [3]. In addition, one can clearly see that the first heating process in the DSC curves—displaying three broad endothermic peaks at ca. 280 ˚C, 330 ˚C, and 470 ˚C—was distinctly different from the next nine heating processes which only showed one sharp peak at ca. 270 ˚C (Fig. 5(a)).

In order to further study the phase transformation process of $BiVO_4$ near the temperature of the color change, the variable-temperature XRD patterns were recorded. According to the endothermic and exothermic peaks in the first two DSC cycles for $BiVO_4$ quantum tubes (Fig. 5(a)), the XRD patterns at a series of temperature points around the peak temperatures such as 20 ˚C, 250 ˚C, 260 ˚C, 270 ˚C, 500 ˚C, 140 ˚C, 130 ˚C, and 120 ˚C (Fig. 6(a) and Fig. S-4(a) in the ESM) for the first cycle, and 250 ˚C, 260 ˚C, 270 ˚C, 140 ˚C, 130 ˚C, and 120 ˚C (Fig. 6(b) and Fig. S-4(b) in the ESM) for the second cycle were recorded. It is well known, that extent of peak splitting at $2\theta = 18.5°$, 35°, 46° or 59° can be used to differentiate between monoclinic and tetragonal scheelite phases of $BiVO_4$ [6, 27, 28]. For the first cycle, as depicted in Fig. 6(a) and Fig. S-4(a) in the ESM, the XRD peak at $2\theta = 35°$ gradually changed from being obviously split to unsplit when the sample was heated from 250 ˚C to 270 ˚C, indicating that a gradual phase transformation from the monoclinic to the tetragonal phase of $BiVO_4$ had taken place during the heating; meanwhile, when the temperature was decreased from 140 ˚C to 120 ˚C, the single XRD peak at $2\theta = 35°$ gradually split into two peaks, suggesting that the tetragonal $BiVO_4$ gradually reverted to the monoclinic phase. In the second cycle, as shown in Fig. 6(b) and Fig. S-4(b) in the ESM, the same monoclinic to tetragonal phase transformation process was observed when the sample was heated from 250 ˚C to 270 ˚C, and the tetragonal phase reverted to the monoclinic form when cooled to 120 ˚C from 140 ˚C. Since the same phase change process occurred in the heating and cooling processes of the first two DSC cycles, the origin of the differences between the first two heating DSC curves prompts the following questions: why are there differences for the same monoclinic to tetragonal phase change process? Are there some external substances which are responsible for the change of peak shape?

To answer these questions, the variable-temperature IR spectra, TGA, and variable-temperature XRD patterns were used to give a more in-depth understanding of the differences between the first two heating DSC curves. Thus, as shown in Figs. 6(c) and 6(d), the peaks in the IR spectrum between 1350 and 1600 cm^{-1}, corresponding to $\upsilon(COO^-)$ stretches of oleate ions [29], did not display any obvious change when the sample was

heated from 20 ℃ to 300 ℃, whereas they gradually disappeared when the sample was heated from 300 ℃ to 500 ℃, implying the gradual volatilization or decomposition of oleate ions above 300 ℃. Meanwhile, the two strong IR absorption peaks at ca. 775 cm^{-1} and 723 cm^{-1} (Fig. 6(d)), assigned to υ_1 (VO_4) and υ_3 (VO_4) [30], gradually coalesced to a single peak when the sample was heated from 250 ℃ to 270 ℃, showing that the distorted VO_4 group gradually became regular, as expected for the monoclinic to tetragonal phase change of $BiVO_4$ [31]. Accordingly, the broad peak at ca. 280 ℃ in the first heating DSC curve can be attributed to the endothermic monoclinic to tetragonal phase change of $BiVO_4$, while the broad peaks at ca. 330 ℃ and 470 ℃ can be assigned to the volatilization or decomposition of oleate ions. This conclusion was further supported by the corresponding TGA and variable-temperature XRD results. As depicted in Fig. 6(e), there was a rapid mass loss in the temperature range 300 ℃ to 500 ℃; the corresponding variable-temperature XRD patterns (Fig. 6(f) and Fig. S-4(c) in the ESM) clearly show that tetragonal

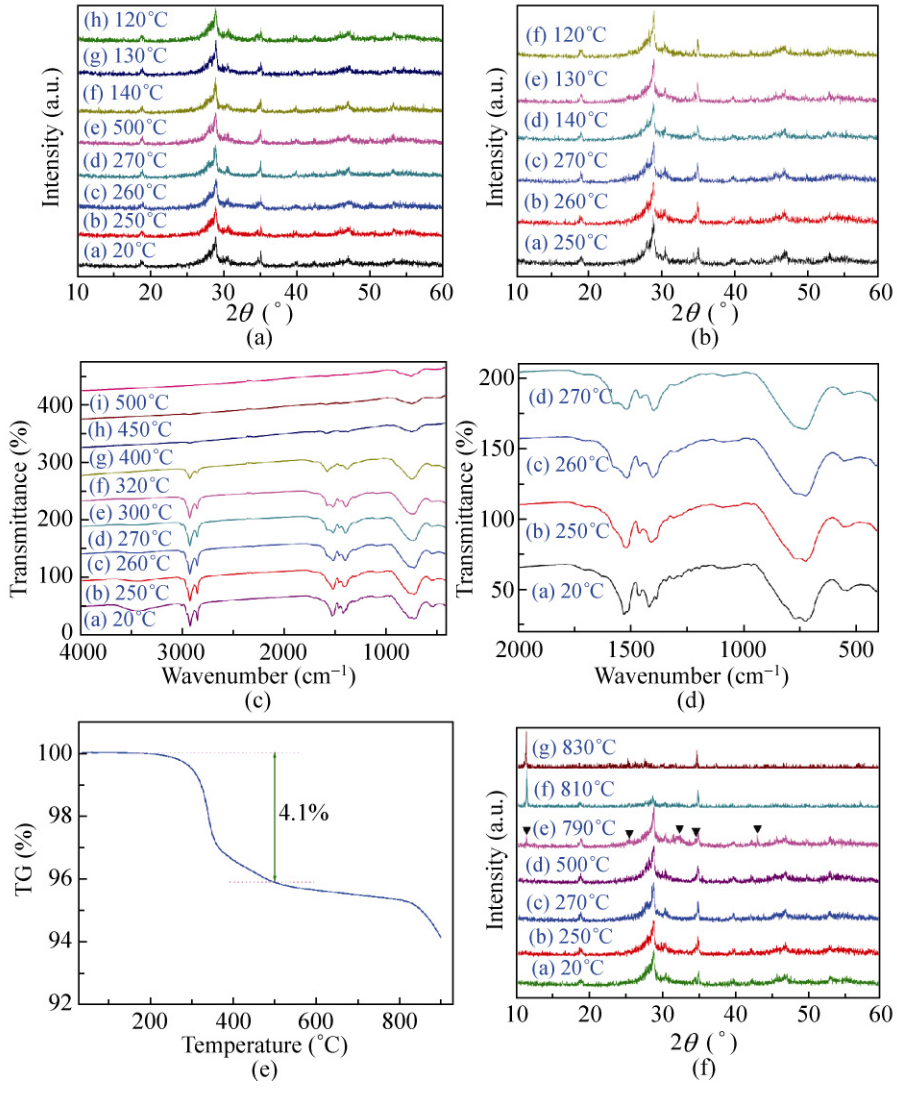

Figure 6 Characterization of the m-$BiVO_4$ quantum tubes: (a, b) the variable-temperature XRD patterns corresponding to the first and second DSC cycles, respectively, in Fig. 5(a); (c) the variable-temperature IR spectra between 20 ℃ and 500 ℃; (d) expanded variable-temperature IR spectra between 20 ℃ and 270 ℃; (e) a typical TGA curve measured between 20 ℃ and 900 ℃ with a heating rate of 10 ℃·min^{-1} in N_2; (f) the variable-temperature XRD patterns between 20 ℃ and 830 ℃

$BiVO_4$ (t-$BiVO_4$), formed from the monoclinic phase by a phase change at ca. 250 ˚C, is stable at temperatures between 270 ˚C and 500 ˚C, suggesting that the rapid mass loss of ca. 4.1% in the TGA analysis can only stem from the volatilization or decomposition of oleate ions. Consequently, the broad peaks at ca. 330 ˚C and 470 ˚C in the TGA can indeed be attributed to endothermic peaks associated with the volatilization or decomposition of oleate ions, which results in broadening of the endothermic peak at 280 ˚C associated with the monoclinic to tetragonal phase change in the first heating DSC curve (Fig. 5(a)). Additionally, another mass loss above 810 ˚C can be observed in the TGA trace (Fig. 6(e)), corresponding to the decomposition of m-$BiVO_4$ to $Bi_{17}V_3O_{33}$, indicating that the thermal stability of the m-$BiVO_4$ quantum tubes was significantly improved compared with that of m-$BiVO_4$ nanoellipsoids, which decompose at ca. 620 ˚C [32].

More importantly, as illustrated in Fig. 5(a), the $BiVO_4$ quantum tubes showed significantly higher endothermic and exothermic enthalpies in their DSC traces than bulk $BiVO_4$ [3], associated with a large heat hysteresis. The reduced size and dimensionality of the quantum tubes result in numerous interfaces between contiguous crystallites, hence, greatly increasing their interfacial energy. Thus, in the heating process the quantum tubes need to absorb more energy in order to overcome the high energy barrier and consequently release more heat energy in the cooling process. This not only increases their phase transition enthalpy but also delays their phase change temperatures, thus, leading to much larger endothermic/exothermic peaks together with a wide hysteresis. Accordingly, the m-$BiVO_4$ quantum tubes not only display a more noticeable color change between bright-yellow and brick-red, but also have a much wider difference between the transition temperatures from the high-temperature brick-red t-$BiVO_4$ to the low-temperature bright-yellow m-$BiVO_4$. Since the m-$BiVO_4$ quantum tubes displayed a more striking color change with an excellent cyclability and a much wider temperature range, owing to their extremely small size, huge surface area and tube-like structure, they are highly promising materials for application as environment-friendly temperature indicators in a variety of devices and should lead to improved safety.

4. Conclusions

A novel assembly–fusion approach for fabricating mesostructured m-$BiVO_4$ quantum tubes, with ultranarrow diameter of 5 nm, ultrathin wall thickness down to 1 nm and exposed {020} facets, has been developed. The driving force behind the formation of quantum tubes with ultrathin wall thickness is the specific Y-shaped arrangement of oleate ions, while the ultranarrow diameter and ordered mesostructure are governed by the bilayer arrangement of oleate ions. The resulting high-quality m-$BiVO_4$ quantum tubes exhibited excellent dual response to visible light and temperature, demonstrating the superiority of quantum-sized nanotubes over the bulk material. This convenient and economic hydrothermal strategy should be capable of being extended to the preparation of other mesostructured inorganic quantum tubes with similar characteristics, with many interesting new properties and potential applications.

Acknowledgements

This work was financially supported by the National Basic Research Program of China (No. 2009CB939901), the National Natural Science Foundation of China (Nos. 90922016 and 10979047), and the Innovative Project of Chinese Academy of Sciences (No. KJCX2-YW-H2O).

Electronic Supplementary Material: Electron diffraction (ED) pattern, low-angle XRD patterns, UV-vis absorption spectra, plots of concentration change of Rhodamine B in the dark, and variable-temperature XRD patterns are available in the online version of this article at http://dx.doi.org/10.1007/s12274-010-0022-8 and accessible free of charge.

References

[1] Zintl, E.; Varino, L. Process for the manufacture of pure bismuth vanadate. German Patent 422947, 1925.

[2] Granzin, J.; Pohl, D. Refinement of pucherite, $BiVO_4$. Z. Kristallogr. **1984**, *169*, 289–294.

[3] Sun, Y. F.; Wu, C. Z.; Long, R.; Cui, Y.; Zhang, S. D.; Xie, Y. Synthetic loosely packed monoclinic $BiVO_4$ nanoellipsoids with novel multiresponses to visible light, trace gas and temperature. *Chem. Commun.* **2009**, 4542–4544.

[4] Bierlein, J. D.; Sleight, A. W. Ferroelasticity in $BiVO_4$. *Solid State Comm.* **1975**, *16*, 69–70.

[5] Lim, A. R.; Choh, S. H.; Jang, M. S. Ferroelastic phase transition of $BiVO_4$ studied by ^{51}V NMR. *Ferroelectrics* **1989**, *94*, 389–394.

[6] Tokunaga, S.; Kato, H.; Kudo, A. Selective preparation of monoclinic and tetragonal $BiVO_4$ with scheelite structure and their photocatalytic properties. *Chem. Mater.* **2001**, *13*, 4624–4628.

[7] Zhao, Y.; Xie, Y.; Zhu, X.; Yan, S.; Wang, S. X. Surfactant-free synthesis of hyperbranched monoclinic bismuth vanadate and its applications in photocatalysis, gas sensing, and lithium-ion batteries. *Chem. Eur. J.* **2008**, *14*, 1601–1606.

[8] Peng, X. Green chemical approaches toward high-quality semiconductor nanocrystals. *Chem. Eur. J.* **2002**, *8*, 335–339.

[9] Donegá, C. D. M.; Liljeroth, P.; Vanmaeklbergh, D. Physicochemical evaluation of the hot-injection method, a synthesis route for monodisperse nanocrystals. *Small* **2005**, *1*, 1152–1162.

[10] Li, G. S.; Zhang, D. Q.; Yu, J. C. Ordered mesoporous $BiVO_4$ through nanocasting: A superior visible light-driven photocatalyst. *Chem. Mater.* **2008**, *20*, 3983–3992.

[11] Huo, Z. Y.; Tsung, C. H.; Huang, W. Y.; Fardy, M.; Yan, R. X.; Zhang, X. F.; Li, Y. D.; Yang, P. D. Self-organized ultrathin oxide nanocrystals. *Nano Lett.* **2009**, *9*, 1260–1264.

[12] Huo, Z. Y.; Tsung, C. H.; Huang, W. Y.; Zhang, X. F.; Yang, P. D. Sub-two nanometer single crystal Au nanowires. *Nano Lett.* **2008**, *8*, 2041–2044.

[13] Du, Y. P.; Zhang, Y. W.; Yan, Z. G.; Sun, L. D.; Yan, C. H. Highly luminescent self-organized sub-2-nm EuOF nanowires. *J. Am. Chem. Soc.* **2009**, *131*, 16364–16265.

[14] Kameshima, Y.; Yoshizaki, H.; Nakajima, A.; Okada K. Preparation of sodium oleate/layered double hydroxide composites with acid-resistant properties. *J. Colloid Interf. Sci.* **2006**, *298*, 624–628.

[15] Messer, B.; Song, J. H.; Huang, M.; Wu, Y. Y.; Kim, F.; Yang, P. D. Surfactant-induced mesoscopic assemblies of inorganic molecular chains. *Adv. Mater.* **2000**, *12*, 1526–1528.

[16] Penn, L.; Banfield, J. F. Imperfect oriented attachment: Dislocation generation in defect-free nanocrystals. *Science* **1998**, 281, 969–971.

[17] Nisar, A.; Zhuang, J.; Wang, X. Cluster-based self-assembly: Reversible formation of polyoxometalate nanocones and nanotubes. *Chem. Mater.* **2009**, *21*, 3745–3751.

[18] Li, H.; Sun, H.; Qi, W.; Xu, M.; Wu, L. Onionlike hybrid assemblies based on surfactant-encapsulated polyoxometalates. *Angew. Chem. Int. Ed.* **2007**, *46*, 1300–1303.

[19] Polleux, J.; Pinna, N.; Antonietti, M.; Niederberger, M. Growth and assembly of crystalline tungsten oxide nanostructures assisted by bioligation. *J. Am. Chem. Soc.* **2005**, *127*, 15595–15601.

[20] Tang, Z. Y.; Kotov, N. A.; Giersig, M. Spontaneous organization of single CdTe nanoparticles into luminescent nanowires. *Science* **2002**, *297*, 237–240.

[21] Niederberger, M.; Cölfen, H. Oriented attachment and mesocrystals: Non-classical crystallization mechanisms based on nanoparticle assembly. *Phys. Chem. Chem. Phys.* **2006**, *8*, 3271–3287.

[22] Oshikiri, M.; Boero, M.; Ye, J. H.; Zou, Z. G.; Kido, G. Electronic structures of promising photocatalysts $InMO_4$ (M = V, Nb, Ta) and $BiVO_4$ for water decomposition in the visible wavelength region. *J. Chem. Phys.* **2002**, *117*, 7313–7318.

[23] Tang, J.; Zou, Z.; Ye, J. Efficient photocatalytic decomposition of organic contaminants over $CaBi_2O_4$ under visible-light irradiation. *Angew. Chem. Int. Ed.* **2004**, *43*, 4463–4466.

[24] Yu, J.; Kudo, A. Effects of structural variation on the photocatalytic performance of hydrothermally synthesized $BiVO_4$. *Adv. Funct. Mater.* **2006**, *16*, 2163–2169.

[25] Tang, J.; Zou, Z.; Ye, J. Effects of substituting Sr^{2+} and Ba^{2+} for Ca^{2+} on the structural properties and photocatalytic behaviors of $CaIn_2O_4$. *Chem. Mater.* **2004**, *16*, 1644–1649.

[26] Linsebigler, A. L.; Lu, G. Q.; Yates, J. T. Photocatalysis on TiO_2 surfaces—principles, mechanisms, and selected results. *Chem. Rev.* **1995**, *95*, 735–758.

[27] Zhang, L.; Chen, D.; Jiao, X. Monoclinic structured $BiVO_4$ nanosheets: Hydrothermal preparation, formation mechanism, and coloristic and photocatalytic properties. *J. Phys. Chem. B* **2006**, *110*, 2668–2673.

[28] Zhou, L.; Wang, W. Z.; Zhang, L. S.; Xu, H. L.; Zhu, W. Single-crystalline $BiVO_4$ microtubes with square cross-sections: Microstructure, growth mechanism, and photocatalytic property. *J. Phys. Chem. C* **2007**, *111*, 13659–13664.

[29] Li, C. H.; Peng, Q.; Li, Y. D. Controlled synthesis of nearly monodispersed $Mn_2(PO_4)Cl$ nanocrystals and nanorods. *Cryst. Growth Des.* **2008**, *8*, 243–246.

[30] Liu, J. B.; Wang, H.; Wang, S.; Yan, H. Hydrothermal preparation of $BiVO_4$ powders. *Mater. Sci. Eng. B* **2003**, *104*, 36–39.

[31] Borisov, S. M.; Vasylevska, A. S.; Krause, C.; Wolfbeis, O. S. Composite luminescent material for dual sensing of oxygen and temperature. *Adv. Funct. Mater.* **2006**, *16*, 1536–1542.

[32] Sun, Y. F.; Xie, Y.; Wu, C. Z.; Long, R. First experimental identification of $BiVO_4{\cdot}0.4H_2O$ and its evolution mechanism to final monoclinic $BiVO_4$. *Cryst. Growth Des.* **2010**, *10*, 602–607.